Journal of Power Sources 196 (2011) 8048–8056

Contents lists available at ScienceDirect

Journal of Power Sources

journal homepage: www.elsevier.com/locate/jpowsour

The effect of wetting properties on bubble dynamics and fuel distribution in the flow field of direct methanol fuel cells

T. Hutzenlaub[a,*], N. Paust[b], R. Zengerle[a,b], C. Ziegler[a]

[a] Laboratory for MEMS Applications, Department of Microsystems Engineering – IMTEK, University of Freiburg, Georges-Koehler-Allee 106, D-79110 Freiburg, Germany
[b] Hahn-Schickard-Gesellschaft for Applied Research, Wilhelm-Schickard-Straße 10, D-78052 Villingen-Schwenningen, Germany

ARTICLE INFO

Article history:
Received 27 April 2011
Accepted 25 May 2011
Available online 1 June 2011

Keywords:
Fuel cell
DMFC
Contact angle hysteresis
Wetting properties
Bubble dynamics
Flow field

ABSTRACT

We investigate CO_2 bubble dynamics on the anode side of a direct methanol fuel cell (DMFC). In contrast to previous studies, we analyse the effect of both channel wall and diffusion layer wettability by observing two-phase flow from the side at different mean velocities of the fuel supply. Hydrophobic and hydrophilic flow channel surfaces are compared experimentally. The hydrophilic flow channel leads to a minimum pressure drop along the channel. Bubbles show virtually no pinning and consequently travel at approximately the mean fuel velocity inside the channel. In contrast to this, we observe bubble pinning in the hydrophobic flow channels. The critical fuel velocities necessary for detachment of the bubbles mainly depends on bubble length. We identify and describe a new bubble bypass configuration where fuel bypass channels are solely generated in a favourable position underneath a blocking bubble along the diffusion layer. This enforces fuel to bypass the CO_2 bubble at a large relative velocity close to the diffusion layer, thus enhancing mass transfer. Our experimental findings are in excellent agreement with a CFD/analytical model. This model allows for quantitative prediction of average bypass flow velocity.

1. Introduction

Comparing hydrogen-fed polymer electrolyte membrane fuel cells (PEMFCs) with direct methanol fuel cells (DMFCs), the latter offer some unique advantages, that have recently led to commercially available systems focusing on off-grid applications. The most notable gain is the simpler fuel storage and refilling, as the liquid methanol solution employed in DMFCs is much more convenient to handle than highly volatile hydrogen [1].

Nevertheless, there are also disadvantages. While PEMFCs employ a pure gas with ideally no waste production on the anode side, the methanol used in DMFCs must be diluted to a concentration of approximately one molar methanol in water to mitigate the losses from methanol crossover [2]. Additionally, CO_2 is produced as a waste gas, creating two-phase flow including blocking bubbles, with the void fraction increasing along channel length, as first observed by Argyropoulos et al. [3]. This leads to a much more complicated anodic mass transfer system and to higher mass transfer losses as current density increases. As a result, the current density of a DMFC is lower than that of a conventional PEMFC, due to higher losses on the anode side [4].

Actively transporting liquid instead of pure gas through the flow field of a fuel cell causes additional system losses due to an increase of necessary pumping energy. The pressure drop can be predicted and optimised only by considering two-phase flow, as the pressure drop induced by blocking bubbles due to interfacial forces between liquid and gas is significant and cannot be neglected [5]. Therefore understanding bubble behaviour is of special interest for design and analysis of liquid feed direct methanol fuel cells.

A common method for analysing two-phase flow in fuel cells is visualisation in a transparent flow field which allows a top view of parts or the whole flow field [3,6–8]. An alternative method presented in [9] detects void fraction, slug velocity and liquid slug length at the exit of a DMFC anode flow field. Similar techniques are also employed in general microfluidics [10–15]. Fuerstman et al. [16] derive the pressure drop in a rectangular micro-channel with flowing liquid and blocking bubbles dependent on channel aspect ratio and the liquid used. Zhu and Petkovic-Duran [17] observe interface velocity when employing different channel materials and surface treatment methods.

Instead of regarding pressure losses due to pinning bubbles in DMFCs to be a major drawback, some groups utilise two-phase flow to circulate fuel in a completely passive manner. They employed buoyancy [18] or tapered channel structures [19,20] to supply the fuel to DMFCs. A disadvantage of this solution is the lower current density due to decreased fuel velocity in the flow channels, which increases mass transfer losses.

* Corresponding author. Tel.: +49 761 203 7238; fax: +49 761 203 7539.
E-mail address: tobias.hutzenlaub@hsg-imit.de (T. Hutzenlaub).

0378-7753/$ – see front matter © 2011 Elsevier B.V. All rights reserved.
doi:10.1016/j.jpowsour.2011.05.070

Nomenclature

A_{chan}	open channel cross-sectional area (m^2)
A_{cor}	bubble bypass cross-sectional area (m^2)
C	correction coefficient for flow resistance of non-circular channel cross-sections
Ca	capillary number
d	thickness of Toray TP-060 diffusion layer (0.19 mm)
F	Faraday constant (F = 96,485 C mol^{-1})
h_{bub}	bubble height, distance between diffusion layer and channel floor (m)
h_{cor}	bubble bypass height along channel wall (m)
i_{max}	maximum intrusion of diffusion layer material into channel (m)
i_{min}	minimum intrusion of diffusion layer material into channel (m)
I	electric current (A)
I_v	bypass flow rate ($m^3\ s^{-1}$)
K	curvature of an interface between two different fluids (m^{-1})
k	in-plane permeability of Toray TP-060 diffusion layer ($1.26 \times 10^{-11}\ m^2$)
l	channel length touching active area (m)
l_{bub}	bubble length from tip to tip in flow direction (m)
l_{cor}	bubble bypass length (m)
$\dot{m}_{CH_3OH}$	mass flow of methanol ($kg\ s^{-1}$)
M_{CH_3OH}	molar mass of methanol ($kg\ mol^{-1}$)
p	static pressure (Pa)
p_c	capillary pressure drop over an interface between two different fluids (Pa)
$p_{c,b}$	capillary pressure drop over the back interface of a bubble (Pa)
$p_{c,f}$	capillary pressure drop over the front interface of a bubble (Pa)
Δp	pressure drop (Pa)
Δp_{bub}	capillary pressure drop over a blocking bubble (Pa)
Δp_{byp}	capillary pressure drop in a bypass along a blocking bubble (Pa)
Q_{DL}	lateral flow rate in the diffusion layer ($m^3\ s^{-1}$)
Q_{SP}	flow rate generated by the syringe pump ($m^3\ s^{-1}$)
v	velocity vector
v_{bub}	bubble velocity ($m\ s^{-1}$)
v_{chan}	average channel velocity ($m\ s^{-1}$)
v_{cor}	average bypass fluid velocity ($m\ s^{-1}$)
w_{bub}	bubble width, $=w_{chan}$ (m)
w_{chan}	channel width (m)
z	valency number
η	dynamic viscosity (2-molar methanol solution: 0.001212 Pa s)
$\theta_{ad,DL}$	advancing contact angle of 2-molar methanol solution on diffusion layer (°)
$\theta_{ad,dyn}$	advancing dynamic contact angle (°)
$\theta_{ad,stat}$	advancing static contact angle (°)
$\theta_{ad,w}$	advancing contact angle of 2-molar methanol solution on channel wall (°)
$\theta_{rec,DL}$	receding contact angle of 2-molar methanol solution on diffusion layer (°)
$\theta_{rec,w}$	receding contact angle of 2-molar methanol solution on channel wall (°)
ρ	density (2-molar methanol solution: 988 $kg\ m^{-3}$)
σ	surface tension (2-molar methanol solution: 0.059 $N\ m^{-1}$)
Ω_i	subdomain i
$\delta\Omega_i$	boundary condition i

One can conclude that an optimum between losses due to pressure drop and mass transfer losses must be found to achieve the maximum efficiency of the system. With this goal in mind, we study bubble dynamics in a DMFC and employ a new visualisation technique by observing the flow field from the side.

In contrast to previous studies, we take into account the difference in wettability between the channel wall and the diffusion layer. We compare a native cyclic olefin copolymer (COC) channel, which is hydrophobic, with a COC channel coated with PDMAA-BP, which is hydrophilic. We vary the mean fuel velocity and observe pinning, contact angle hysteresis, bubble velocity, bubble blocking and bypassing flow to gain a deeper understanding of two-phase flow and its consequences on pressure drop and mass transfer losses in DMFCs.

The experimental work is supported by a dynamic two-phase model. In recent years, different approaches have been presented to model two-phase flow such as Lattice Boltzman [21], dissipative particle dynamics (DPD) [22], molecular dynamics [23] or the standard fluid simulation method based on finite volumes, which is also referred to as computational fluid dynamics (CFD) [24–26]. Especially the last method has gained considerable popularity in the DMFC community due to its capability not only to model two-phase flow, but also to include interacting mechanisms such as electrochemical kinetics or heat transfer by coupling several transport equations [27,28]. In the work reported here, we employ a CFD/analytical model to quantify fuel transport in the bypasses along a blocking bubble in the channel of a DMFC.

2. Experimental

2.1. DMFC setup

To prevent interference by neighbouring channels, a single channel flow field is fabricated of COC. The side wall is polished to achieve optical transparency and the resulting side view of the experiments in the anode flow field channel is documented on film using a magnifying lens and a μEye camera. This flow field is integrated into a fuel cell as illustrated in Fig. 1. A passive cathode fabricated of SGL porous graphite plate is used, and diffusion layers (Toray TP-060) ensure a more even fuel distribution on both the anode and the cathode sides. A catalyst-coated Nafion 115 membrane (active area: 2.6 cm^2; anode: 3 mg cm^{-2} PtRu; cathode: 1.3 mg cm^{-2} Pt; manufactured by BalticFuelCells) provides separation of the two half-cells. As described in [20], contacting is achieved by a 100 μm thick gold foil covering land. Two endplates made of brass on the cathode side and a double layer of PMMA and aluminium on the anode side provide contact pressure. The anode endplate is designed with a viewing window to allow an additional top view of the flow field. Two flow channels with different wettability properties are compared. This is achieved by treating one of the COC flow fields with PDMAA-BP, which creates a more hydrophilic surface. On the anode side, a small load of 0.9 mA mm^{-2} induces CO_2 production. A 2-molar methanol solution is pumped back and forth with a syringe pump. Over time, a channel-blocking bubble grows. After the bubble reaches a specific size, the load is turned off and the dynamic behaviour of the bubble in the channel can be observed at different fluid velocities.

2.2. Microfluidics of two-phase channel flow

The average velocity of methanol solution in the flow channel is derived from the volumetric flow rate of the syringe pump and the channel cross-sectional area. To calculate the exact channel cross-sectional area, the width from the left to the right channel wall and the height from the floor to the top of the employed channels

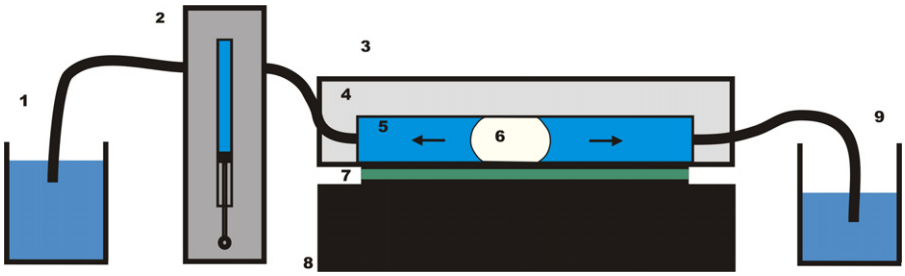

Fig. 1. Schematic diagram of experimental setup: (1) reservoir 1, (2) syringe pump, (3) DMFC, (4) transparent (COC) anode (5) side view of flow channel, (6) blocking bubble (7) membrane and diffusion layers (8) cathode (9) reservoir 2.

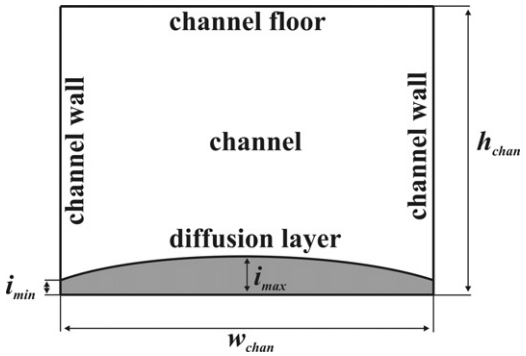

Fig. 2. Schematic diagram of channel cross-section area after clamping, with diffusion layer intrusion *i*. The channel width w_{chan} amounts to 1.135 mm (native COC channel) and 1.170 mm (COC channel coated with PDMAA-BP), the channel heights h_{chan} are determined to be 0.880 mm and 0.910 mm respectively.

are measured after milling. We expect the pressure of clamping to push parts of the diffusion layer into the channel and thus reduce the channel cross-sectional area as depicted in Fig. 2. To quantify this intrusion, we employ a Tesa-Visio 300 video measuring machine to measure the intrusion in situ through the top viewing window of the anode. The highest diffusion layer intrusion of 50 μm is measured in the middle of the channel (Fig. 3). At the edge of the channel, where the diffusion layer reaches land, the intrusion is still about 20 μm due to material being pressed up along the channel wall as can be observed in [29].

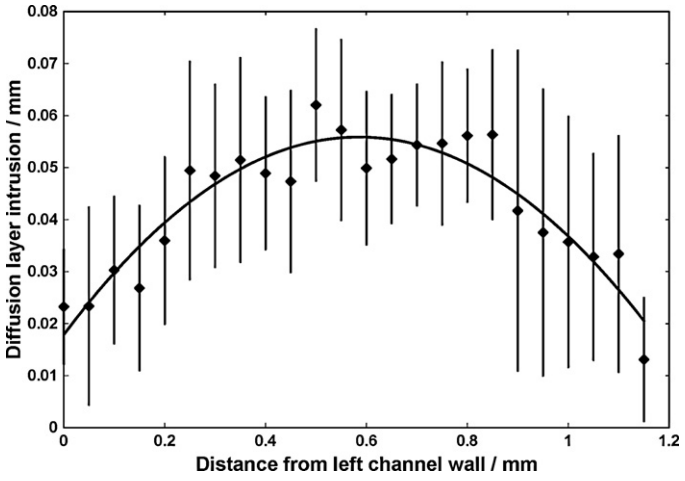

Fig. 3. Diffusion layer material intrusion into the channel coated with PDMAA-BP. The intrusion is measured in situ with a Tesa-Visio 300 video measuring instrument. The minimum intrusion of 20 μm occurs directly along the channel walls, the maximum intrusion is measured in the middle of the channel. Error bars indicate one standard deviation. The error is large due to surface roughness of the diffusion layer.

The cross-sectional area of the uncoated channel is determined to be 0.95 mm^2, the cross-sectional area of the channel coated with PDMAA-BP amounts to 1.02 mm^2 (Fig. 3).

Part of the fuel stream passes through the diffusion layer and thus further reduces the fluid velocity in the flow field channel. This flow rate Q_{DL} can be estimated by rewriting Darcy's Law, where η is the dynamic viscosity of the 2-molar methanol solution, l is the channel length touching the active area and thus the diffusion layer, and w_{chan} is the channel width. k is the in-plane permeability [30] and d the thickness of the employed Toray TP-060 diffusion layer. Δp is the pressure loss over the channel length. In channels with hydrophobic walls, this is mainly dominated by the capillary pressure loss over the blocking bubble, so we assume that $\Delta p = \Delta p_{bub}$:

$$Q_{DL} = \frac{k w_{chan} d}{\eta l} \Delta p_{bub} \tag{1}$$

Thus, the average fuel velocity v_{chan} in the employed flow field channel can be calculated as

$$v_{chan} = \frac{Q_{SP} - Q_{DL}}{A_{Chan}} \tag{2}$$

with the flow rate generated by the syringe pump Q_{SP} and the open channel cross-sectional area A_{chan}. In the channel with the PDMAPP coating, Δp is close to zero and thus we expect only negligible diffusion layer flow.

The syringe pump is calibrated to generate a fuel flow rate between 0 and 15.6 μl s^{-1} which leads to average fuel velocities of 0–16.3 mm s^{-1} in the uncoated channel and 0–15.3 mm s^{-1} mm in the coated channel. These are typical velocities for DMFCs, as is verified by employing Faraday's Law:

$$\dot{m}_{CH_3OH} = \frac{M_{CH_3OH} I}{zF} \tag{3}$$

where the mass flow of methanol $\dot{m}_{CH_3OH}$ consumed by the reaction is calculated from the generated current I, the molar mass of methanol M_{CH_3OH}, the Faraday constant F and the valency number z. For example, using a single-channel meander flow field with a width of 1 mm and a height of 1 mm, a typical current density of 100 mA cm^{-2} [31] and a 2-molar methanol solution pumped at a typical stoichiometry of 5 [32] through an active area of 25 cm^2 would lead to an average fuel velocity of 10.8 mm s^{-1}.

The pressure drop over a single blocking bubble is calculated using the Young–Laplace equation for the difference in pressure p_c across the interface between two different fluids with the interfacial tension σ and the local curvature K:

$$p_c = \sigma K \tag{4}$$

The pressure drop of a bubble can be subsequently formulated as:

$$\Delta p_{bub} = p_{c,f} - p_{c,b} \tag{5}$$

$p_{c,f}$ and $p_{c,b}$ describe the difference in pressure across the liquid/gas interface at the front and the back of the bubble, respectively. These

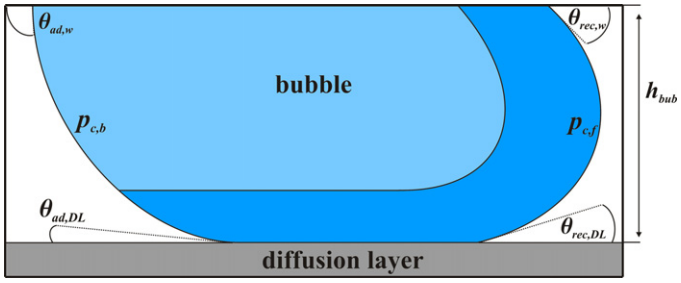

Fig. 4. Schematic diagram of a pressure drop over a blocking bubble, which is derived by subtraction of the pressure drop across the meniscus at the front of the bubble from the pressure drop across the meniscus at the back of the bubble. These are in turn calculated from contact angles and the bubble width and height.

can be derived from the principal curvatures between the left channel wall and the right channel wall and between the channel floor and the diffusion layer:

$$p_{c,f} = \sigma\left(\frac{\cos(\theta_{rec,w})+\cos(\theta_{rec,DL})}{h_{bub}} + \frac{2\cos(\theta_{rec,w})}{w_{bub}}\right) \quad (6)$$

$$p_{c,b} = \sigma\left(\frac{\cos(\theta_{ad,w})+\cos(\theta_{ad,DL})}{h_{bub}} + \frac{2\cos(\theta_{ad,w})}{w_{bub}}\right) \quad (7)$$

with the height h_{bub} and width w_{bub} of the bubble in the channel, and advancing (*ad*) and receding (*rec*) contact angles θ on the wall (*w*) and the diffusion layer (*DL*) (Fig. 4).

Contact angles of the flow field are determined using the sessile drop method. A droplet of the methanol solution used in the DMFC was applied to both COC with a PDMAA-BP coating and native, uncoated COC. Advancing (pre-wetted) and receding contact angles were determined. On the native COC, an advancing contact angle of $68^\circ \pm 3^\circ$ and a receding contact angle of $45^\circ \pm 3^\circ$ were measured. On the COC coated with PDMAA-BP, the advancing contact angle was determined to be $10^\circ \pm 3^\circ$, the receding contact angle was close to 0°. In addition, both advancing and receding contact angles of the diffusion layer are estimated to be close to 0°, as the experiments in the hydrophilic flow field coated with PDMAA-BP show virtually no pinning of blocking bubbles.

The contact angles used for calculation in this work are assumed to be independent of bubble velocity. At higher bubble velocities, dynamic contact angles would start to play a role and initially, advancing contact angles would increase [33]. The bubble shape would change as the velocity rises further, which would lead to an increase of bubble pressure drop and in consequence to an increase of relative velocity between the bubble and the fuel stream.

We conclude that dynamic contact angles can be neglected in the reported work. This is because we observe no significant shape change once the bubble is in motion (Fig. 5). We estimate the dynamic contact angle for a bubble velocity of 15 mm s^{-1} using the formula introduced by Bracke et al. [34]:

$$\cos\ \theta_{ad,dyn} = \cos\ \theta_{ad,stat} - 2(1+\cos\ \theta_{ad,stat})Ca^{0.5} \quad (8)$$

with

$$Ca = \frac{\eta v_{bub}}{\sigma} \quad (9)$$

where the advancing dynamic contact angle $\theta_{ad,dyn}$ is calculated from the corresponding static contact angle $\theta_{ad,stat}$ and the dimensionless velocity expressed as the capillary number *Ca*, which in turn is derived from the dynamic viscosity η and surface tension σ of the liquid and the bubble velocity v_{bub}. For the maximum bubble velocity observed in this experiment, this would increase the advancing contact angle on the channel wall $\theta_{ad,w}$ by 3° from 68° to 71°, which was considered to be negligible.

3. Results

3.1. Pinning and bubble velocity in hydrophilic PDMAA-BP coated COC flow field

Three different blocking bubbles of a total length l_{bub} of 1.4, 2.8 and 4.8 mm (Fig. 6) were generated and the fuel velocity was varied from 0 to 15.3 mm s^{-1}. We observe little pinning for all bubbles. As soon as the fuel feed is activated, the bubbles start to move. As we increase the flow rate, the bubbles equally increase their velocities to match the average fuel velocity.

The bubble geometry is symmetric, with all advancing and receding contact angles being close to 0°, so that both the front of the bubble, in the direction of flow, and the back of the bubble, facing the flow, form a hemisphere with the triple line between the channel floor, methanol solution and CO_2 and the corresponding triple line between the diffusion layer, methanol solution and CO_2 moving in parallel. Small fuel bypass channels around a bubble are formed in all four corners, in accordance with the Concus Finn condition [35]. This states that the sum of both receding contact angles of the surfaces forming a corner and the corner angle is not allowed to be 180° or greater if a bypass in the corner of a channel is to be formed. Considering the two different surface types of channel and diffusion layer, we can formulate the two respective cases:

$$\theta_{rec,DL} + \theta_{rec,w} + \alpha < 180^\circ \quad (10)$$

$$2\theta_{rec,w} + \alpha < 180^\circ \quad (11)$$

In this experiment, all receding angles on both the diffusion layer and the channel wall and floor are close to 0°. With the corner angle of 90° between channel wall and floor and an angle of approximately 83° between diffusion layer and channel wall, due to diffusion layer intrusion into the channel, all sums are clearly lower than 180° and bypass formation is inevitable.

On plotting bubble velocity versus average fuel velocity (Fig. 7), we observe a slope of 1.02 for all bubble sizes, which means that the bubbles travel slightly faster than the average fuel velocity. This can be explained by the parabolic flow profile. Due to the bypasses to the bubble in all four corners of the channel, where the fuel flow is close to the walls and thus flow velocity is considerably lower than in the channel centre, the bubble is in contact with a flow region of higher average velocity than the total average channel velocity.

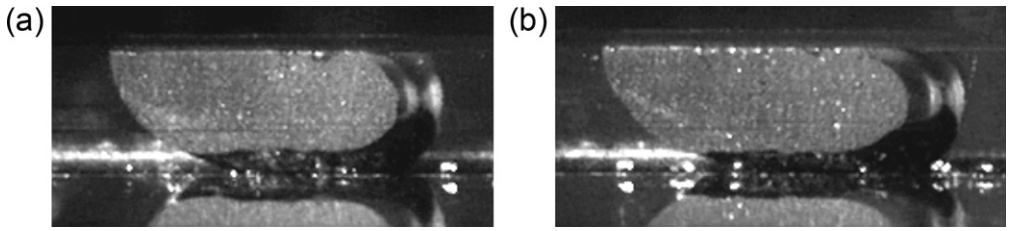

Fig. 5. Bubble geometry at two different average flow velocities inside a native hydrophobic COC channel: (a) 2.6 mm s^{-2}, (b)13.6 mm s^{-2}. The change in the bubble geometry is negligibly small at the investigated fluid velocities. The bubble is depicted schematically in Fig. 6 g.

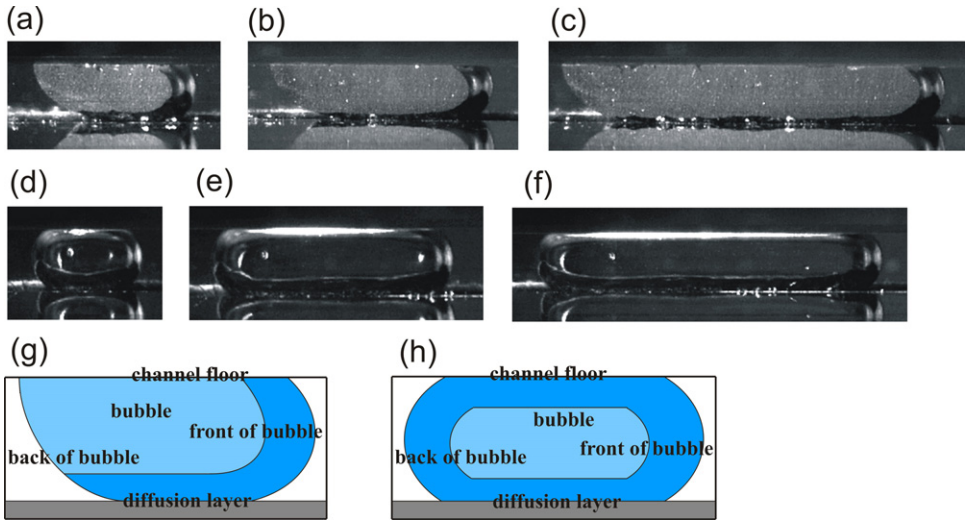

Fig. 6. Bubble observed in experiment at an average flow velocity of 5 mm s^{-2}: (a)–(c) hydrophobic native COC channel, (d)–(f) COC channel coated with hydrophilic PDMAA-BP, (g) schematic diagram of bubble in hydrophobic native COC channel, (h) schematic diagram of bubble in COC channel coated with hydrophilic PDMAA-BP. Bubble length: (a) 2.4 mm (b) 3.2 mm (c) 5.4 mm (d) 1.4 mm (e) 2.8 mm (f) 4.8 mm.

Due to negligible contact angle hysteresis, we do not observe any change in the shape of the bubble when the pumping direction is reversed.

3.2. Bubble pinning and velocity in hydrophobic native COC flow field

Three different blocking bubbles with a total length l_{bub} of 2.4, 3.2 and 5.4 mm (Fig. 6) were generated and the bubble velocity was plotted versus the average fluid velocity (Fig. 8). Observing the smallest, 2.4 mm bubble, we identify three different types of behaviour depending on fuel velocity:

At a low velocity of up to 2 mm s^{-1} we observe pinning, with the contact angle hysteresis increasing at the walls of the channel as the velocity rises. At the front of the bubble, in the direction of flow, the receding contact angle is established. At the back of the bubble, the advancing contact angle is established. In contrast to the diffusion layer, where contact angle hysteresis is negligible, the hysteresis here causes the contact angle at the channel floor to differ significantly between the back and the front of the bubble. Consequently, the shape of the bubble caps is different as illustrated in Fig. 6. At the back of the bubble the part of the meniscus touching the channel floor is pulled back away from the bubble centre so that the receding contact angles of both walls and the diffusion layer can be formed. By contrast, the difference is considerably lower at the front of the bubble so that a cap is formed, which more closely resembles a hemisphere, with the triple line between the channel boundary, methanol solution and CO_2 on the channel floor slightly further forward than the triple line on the diffusion layer. Due to bubble pinning, the methanol solution must bypass the bubble in the corners of the channel. We do not observe any bypass in the corners between the channel walls and floor. Instead, the fuel overtaking the bubble bypasses the bubble in the corners between the channel walls and the diffusion layer, leading to a detachment of most of the meniscus facing the diffusion layer. This effect is further reinforced due to the fact that the diffusion layer arches into the channel, as illustrated in Fig. 2, so that the bubble only rides on a narrow strip in the middle of the diffusion layer. Therefore the main part of the diffusion layer is in direct contact with the methanol solution. With the contact angles measured in Section 2.2, this satisfies the Concus Finn condition already described in Eqs. (10) and (11), where the sum of both receding contact angles of the surfaces forming a corner and the corner angle is not allowed to be 180° or larger so that a bubble bypass in the corner of a channel can be formed.

At 2 mm s^{-1}, the bubble has a fully developed contact angle hysteresis and will retain this shape even at higher velocities as long as the direction of the flow does not change. At a higher velocity than 2 mm s^{-1}, the bubble detaches itself from its pinning position and

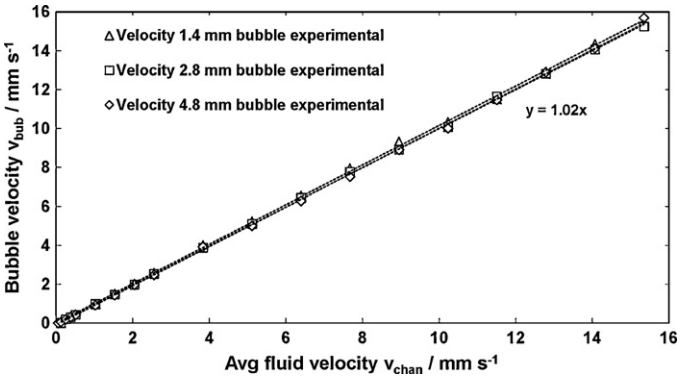

Fig. 7. Bubble velocity versus average flow velocity for 3 bubble lengths in the COC channel coated with hydrophilic PDMAA-BP. We do not observe any pinning. The bubble velocity is independent of bubble length.

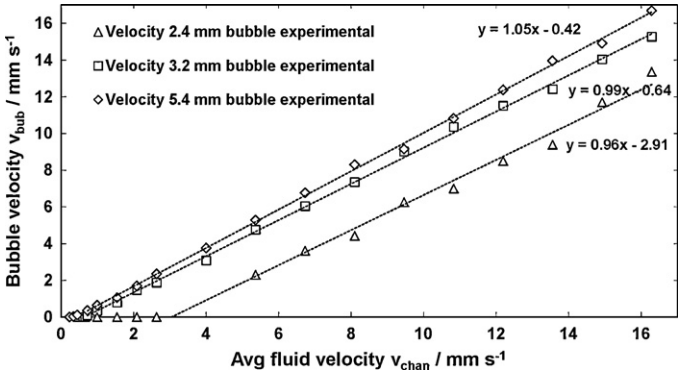

Fig. 8. Bubble velocity versus average flow velocity for 3 bubble lengths in the hydrophobic native COC channel. We observe pinning in dependence on the bubble length. Longer bubbles require a lower average flow velocity to detach themselves from their pinning position.

starts to move in the direction of the flow. Additionally, we observe that between 2 and 3 mm s^{-1}, the bubble is subject to stop-and-go motion, which is attributed to diffusion layer roughness. The bubble movement is assumed to be interrupted by carbon fibres that protrude into the channel.

Above 3 mm s^{-1}, we observe a linear increase of bubble velocity with the average fluid velocity. The gradient is slightly less than one, so the relative velocity between the bubble and the fluid decreases slightly in the velocity range investigated in this work, once the bubble is in motion.

The medium-sized bubble starts moving at considerably lower velocities. We observe pinning between 0 and 0.7 mm s^{-1} fuel velocity. There is no stop-and-go behaviour, the larger bubble copes better with the surface roughness but at 0.7 mm s^{-1} and faster we observe a linear rise of approximately one.

The largest bubble generated starts to move at even lower velocities. We observe pinning merely between 0 and 0.5 mm s^{-1} fuel velocity. There is no stop-and-go behaviour. Starting from 0.5 mm s^{-1} we observe a linear rise of bubble velocity with fluid velocity, with a slope slightly greater than one.

It is noteworthy that the largest bubble, starting at about 15 mm s^{-1}, travels faster than the average channel velocity, a phenomenon observed and explained in Section 3.1. Small and medium bubbles do not show this behaviour.

Additionally, the pumping direction was frequently reversed to observe the change in bubble geometry. As one can expect, advancing and receding contact angles trade locations and the bubble moves in the opposite direction with the same absolute value of relative velocity.

3.3. Impact on mass transport and DMFC performance

The pressure gradient, that is created by the flow to develop and maintain the full contact angle hysteresis against friction [36], and the ability to open bypasses along the bubble, lead to a relative velocity between the gas bubble and the methanol solution, even at fuel velocities that allow no bubble pinning. The decisive factor determining how quickly CO_2 can be transported out of the flow field in any given channel and diffusion layer configuration is the length of the blocking bubble. This configuration can in turn be varied by using different materials to reduce or increase the contact angle. Lower contact angles will not only facilitate bubble transportation but also reduce the pressure drop per blocking bubble. Consequently, the energy lost by the pumping needed to overcome the flow field pressure drop can be decreased by reducing the contact angles of the boundaries enclosing the channel. At first sight, this would identify the channel with the hydrophilic PDMAA-BP coating as the favoured configuration to generate higher power densities.

On second thought, the native COC channel, featuring a highly hydrophilic diffusion layer and a hydrophobic channel, offers a unique advantage compared to the completely hydrophilic configuration. Due to the fact that this configuration yields bypasses only in the corners between the diffusion layer and the channel walls in combination with a high pressure drop between the back and front of the bubble, high fuel velocities can be expected above the diffusion layer under a blocking bubble. This aids methanol transport to and reaction product removal away from the reaction centre, so that mass transfer is enhanced. It is additionally facilitated by the diffusion layer arching into the channel due to the clamping pressure, so that most of the diffusion layer is directly exposed to the fuel stream. This effect increases as the blocking bubble density increases, which offers the additional advantage of enhancing mass transport in dependence on channel length, which compensates for methanol concentration losses due to reaction and crossover.

In contrast to this, bubble transportation in completely hydrophilic channels will only cause a minor disturbance of the typical parabolic flow profile in the middle of the channel and the fuel layer directly above the diffusion layer is mostly stagnant. Thus, the supply of methanol and waste discharge mainly relies on diffusion. To study this further, the generated velocities in the uncoated channel configurations are calculated using a model which is described in the following section.

4. Model

4.1. Description

The model presented is a three-dimensional, two-phase model of a blocking bubble in the flow field channel of a DMFC for the purpose of investigating fuel transport along the boundary between the diffusion layer and the channel. A detailed description of the following phenomena is provided in this section:

(1) Average velocity of methanol solution bypassing the bubbles in the corners between the diffusion layer and channel wall.
(2) Bubble velocity resulting from surface properties, bubble length and mean flow rate of the fuel in the channel.

The main assumptions in this model are as follows:

(1) The model is defined to be isothermal.
(2) All fluids are incompressible.
(3) All flow is laminar.
(4) Concentration changes due to chemical reactions are neglected.
(5) The bubble is considered to be in motion, which means that the contact angle hysteresis is fully developed, and the bubble shape is assumed to be constant and independent of transport velocity.
(6) The channel floor and walls are defined to be no-slip walls.
(7) Bubble menisci are treated as slip boundaries.
(8) Only advancing and receding contact angles are used; a gradual transition over the length of a bypass is not considered. Consequently, a fully developed bypass is defined as a channel with a constant cross-section.

4.2. Model domain, equations and numerical solution

The computational domain employed for the simulation part of this work is depicted in Fig. 9a. The domain represents a section containing one blocking bubble, with the channel cut perpendicularly to the diffusion layer, channel walls and channel floor along the front and back of the bubble. The frame of reference is the gas bubble with the coordinate system fixed at the centre of gravity of the bubble so that the simulation of bubble motion is described by moving walls and corresponding methanol solution flow. The computational domain is divided into subdomains Ω_i with Ω_1 describing the parts of the channel around the bubble filled with methanol solution and Ω_2 defined as the gas bubble. These subdomains are coupled with each other and enclosed by boundary conditions $\delta\Omega_i$. The inlet and outlet of the domain are described by $\delta\Omega_1$ and $\delta\Omega_2$ respectively. Both are defined as constant pressure boundary conditions, with $\delta\Omega_1$ set to the sum of ambient pressure and the pressure drop from inlet to outlet. $\delta\Omega_2$ is set to ambient pressure. $\delta\Omega_3$ describes the bubble meniscus between the methanol solution and CO_2 gas and is defined as a slip boundary. At $\delta\Omega_4$ to $\delta\Omega_7$, no-slip boundary conditions between fuel and wall ($\delta\Omega_4$), fuel and diffusion layer ($\delta\Omega_5$), bubble and wall ($\delta\Omega_6$) and bubble and diffusion layer ($\delta\Omega_7$) are set.

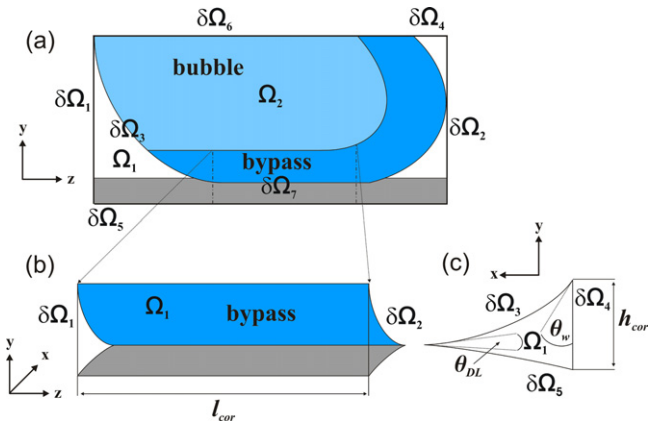

Fig. 9. (a) Model domain: Ω_1: liquid phase Ω_2: gas phase; interfaces: $\delta\Omega_1$: methanol solution inlet $\delta\Omega_2$: methanol solution outlet $\delta\Omega_3$: bubble meniscus between methanol solution and CO_2 gas $\delta\Omega_4$: methanol solution ↔ channel wall $\delta\Omega_5$: methanol solution ↔ diffusion layer $\delta\Omega_6$: CO_2 gas ↔ channel wall $\delta\Omega_7$: CO_2 gas ↔ diffusion layer and (b) we assume that the capillary pressure drop over the gas bubble equals the pressure drop over the bubble bypasses and can thus calculate the volume flow by reconstructing the bypass and using it as our simplified model domain. Model domain: Ω_1: liquid phase; interfaces: $\delta\Omega_1$: methanol solution inlet $\delta\Omega_2$: methanol solution outlet. (c) Cross-section of the domain described in (b)). Model domain: Ω_1: liquid phase; interfaces: $\delta\Omega_3$: bubble meniscus between methanol solution and CO_2 gas $\delta\Omega_4$: methanol solution ↔ channel wall $\delta\Omega_5$: methanol solution ↔ diffusion layer; contact angles: θ_w: methanol solution on COC wall θ_{DL}: methanol solution on diffusion layer.

To reduce calculation time and allow for parametric studies, the model is further simplified by the following assumptions:

The pressure distribution in the gas within the bubble can be considered to be constant.

The capillary pressure drop over the bubble, which has to be matched by the liquid phase of the channel, will mainly occur in the bypasses along the bubble due to their relatively small cross-section compared to the cross-section of the channel. So we assume:

$$\Delta p_{bub} = \Delta p_{byp} \tag{12}$$

with the capillary pressure drop over the bubble Δp_{bub} and the linear pressure drop Δp_{byp} in the bypass channel of the bubble.

The slip boundary can be approximated by a symmetry condition which does not allow any momentum transfer.

These assumptions lead to a simplified domain which is depicted in Fig. 9b and c, where a single bypass Ω_1 containing methanol solution features constant-pressure boundaries at the inlet ($\delta\Omega_1$) and outlet ($\delta\Omega_2$), and symmetric conditions ($\delta\Omega_3$) describe the bubble meniscus, as well as the no-slip walls of the channel ($\delta\Omega_4$) and the diffusion layer ($\delta\Omega_5$).

All densities are considered constant so mass conservation may be reduced to:

$$\nabla \cdot \rho\vec{v} = 0 \tag{13}$$

with the velocity vector $\vec{v}$ and the density of methanol solution ρ.

In general, the velocity field is determined by the Navier–Stokes equation for incompressible fluids:

$$\rho\left(\frac{\partial\vec{v}}{\partial t} + \vec{v}\cdot\nabla\vec{v}\right) = -\nabla p + \eta\nabla^2\vec{v} \tag{14}$$

with the velocity vector $\vec{v}$, the static pressure p and density ρ and viscosity η of the methanol solution. As stated above, our model domain is assumed to be a channel parallel to the z axis with a constant cross-section in the xy-plane (Fig. 9). Consequently, the forces in the xy-plane cancel each other, leading to a velocity field independent of z where only the sum of its z components can be non-zero. So we conclude: $\vec{v}\cdot\nabla\vec{v} = 0$. In analogy to this, the pressure similarly depends only on z and is thus a linear function of z. Due to the fact that the coordinate system is fixed at the centre of gravity of the bubble and we hence only study a progression of velocity fields in steady state, we can additionally assume that $\partial\vec{v}/\partial t$ equals zero. We can now formulate what is commonly known as Hagen–Poiseuille flow [37]:

$$(\partial_x^2 + \partial_y^2)v_z(x,y) = -\frac{\Delta p}{\eta l} \tag{15}$$

with the length l of the channel and the pressure drop Δp from inlet to outlet.

This expression for the velocity field can now be used to derive the volume flow rate in the channel as a function of the pressure drop for an arbitrary cross-sectional shape by the introducing a specific correction coefficient C [37]:

$$I_v = \frac{\Delta p A^2}{l\eta C} \tag{16}$$

As both the volume flow I_v and the correction coefficient C are unknown, we apply CFD to solve this problem numerically, as described in the following section.

4.3. Model validation: comparison of modelling results

The geometrical configuration of the bubble bypass channels is reconstructed from the films of the experiments. The bypass channels are described by the bypass length l_{cor} and bypass height h_{cor}. With the known receding contact angles at the wall $\theta_{rec,w}$ and diffusion layer $\theta_{rec,DL}$, the cross-sectional area A_{cor} is well-defined. The bypass is modelled in the CAD SolidWorks software, imported into the CFD-GEOM meshing tool and meshed with a structured grid consisting of 50,000 to 100,000 cells depending on the size of the bubble bypass channels. We assume that Δp is equal to the capillary pressure drop Δp_{bub} over the bubble, which in turn can be calculated as demonstrated in Section 2.2.

Finally the model is solved by applying the CFD-ACE + simulation software from the ESI Group company [38]. As the bubble serves as the frame of reference, the bubble velocity is described indirectly by moving the walls ($\delta\Omega_4$, $\delta\Omega_5$) against the direction of flow with the desired magnitude of velocity. This procedure can be further simplified by only simulating the transition point between bubble pinning and movement, where the bubble velocity v_{bub} is still zero but the contact angle hysteresis is fully developed. After convergence, a bubble bypass flow rate I_v is calculated and from this, a correction coefficient C for the specific geometric form of the respective cross-section is derived:

$$C = \frac{\Delta p_{bub} A_{cor}^2}{I_v l_{cor}\eta} \tag{17}$$

The starting point to derive the relation between the average fuel velocity in the channel and the bubble velocity is the balance of flow rates between the channel (subscript chan), bypass (subscript cor) and bubble (subscript bub) at the transition point that can be described as:

$$v_{chan}A_{chan} = v_{bub}(A_{chan} - 2A_{cor}) + 2v_{cor}A_{cor} \tag{18}$$

With

$$I_v = v_{cor}A_{cor} \tag{19}$$

and Eq. (17), v_{cor} is substituted in Eq. (18) and a general dependence of the bubble velocity v_{bub} on the average channel velocity v_{chan} can be formulated:

$$v_{bub} = \frac{v_{chan}A_{chan}}{A_{chan} - 2A_{cor}} - \frac{2\Delta p {A_{cor}}^2}{C\eta l_{cor}(A_{chan} - 2A_{cor})} \tag{20}$$

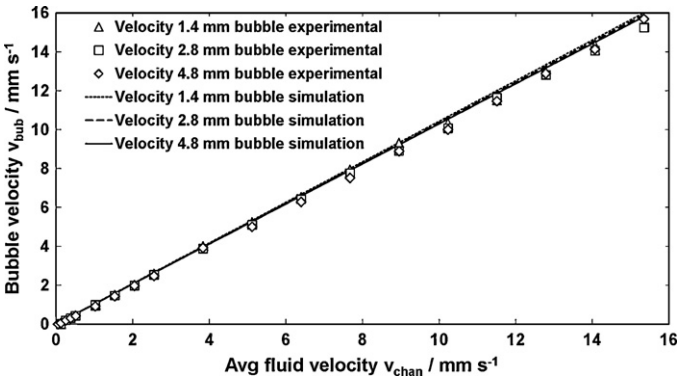

Fig. 10. Comparison of simulation and experiment: Bubble velocity versus average channel velocity for 3 bubble lengths in the COC channel coated with hydrophilic PDMAA-BP. Excellent agreement between simulation and experiment is achieved.

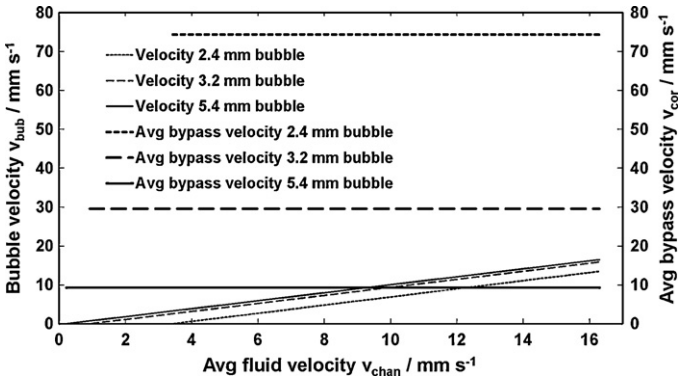

Fig. 12. Simulation results: bubble velocity and average bubble bypass velocity versus average channel velocity for 3 bubble lengths in the hydrophobic native COC channel. Shorter bubbles induce considerably higher fuel velocities in their bypass channels.

This approach is repeated to cover the range of bubble velocities and geometric dimensions observed in the experimental part of this work. Finally the results are compared to the experimental data of both coated (Fig. 10) and uncoated channel (Fig. 11).

Excellent agreement between simulation and experiment is achieved.

4.4. Average fuel velocity bypassing the bubble

We reconsider the hypothesis formulated in Section 3.3, where high velocities of methanol solution in the bubble bypasses of the hydrophobic channel directly above the diffusion layer were predicted. We can now derive a formula to predict the fuel velocity in the bypass of a blocking bubble relative to the channel wall by replacing v_{bub} in Eq. (18) with Eq. (20):

$$v_{cor} = \frac{\Delta p A_{cor}}{C \eta l_{cor}} \tag{21}$$

In conclusion, this means that the relative velocity of the fuel bypassing a blocking but non-pinning bubble is independent of both bubble and mean fuel velocity inside the channel, as soon as contact angle hysteresis and subsequently the pressure loss over the bubble is fully developed. Blocking bubbles in hydrophilic channels with a pressure loss of approximately zero will consequently cause a momentary standstill in fuel transport. Increasing the contact angle hysteresis will lead to higher fuel velocities in this critical zone directly above the diffusion layer.

By analysing the experimentally generated bubbles, we can on the one hand conclude that both viscosity η, due to negligible changes in temperature and substance concentration, and the geometric correction coefficient C, due to lack of significant change in cross-section form, can be regarded as constant values for any given bubble length in our system. On the other hand, the ratio of the bypass cross-sectional area A_{cor} to the bypass length l_{cor} significantly decreases as the blocking bubble increases in length, and subsequently the fuel velocity v_{cor} bypassing the bubble decreases by the same ratio. In the native hydrophobic COC channel analysed in this work, the 2.4 mm long bubble induces a very high average velocity of 74 mm s^{-1} of the fuel in the bypass channel. The velocity decreases as the blocking bubble becomes longer. The 3.2 mm bubble still offers an average velocity of the fuel of 30 mm s^{-1} when the bubble is bypassed. Finally, at 5.4 mm bubble length, a fuel velocity of 9 mm s^{-1} can be achieved (Fig. 12).

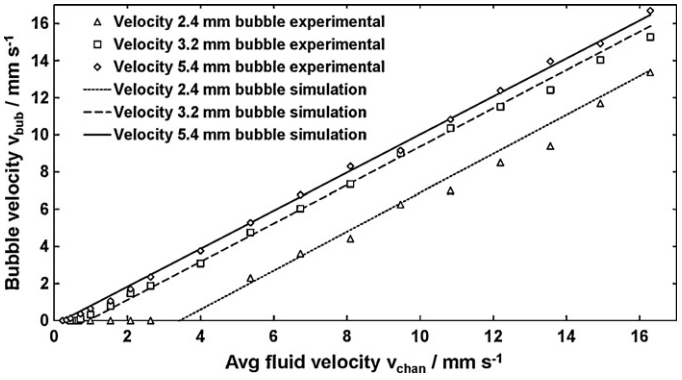

Fig. 11. Comparison of simulation and experiment: Bubble velocity versus average channel velocity for 3 bubble lengths in the hydrophobic native COC channel. Excellent agreement between simulation and experiment is achieved.

5. Conclusion

We visually investigated blocking CO_2 bubbles as they occur in the anode of a direct methanol fuel cell (DMFC). For the first time, we provide a side view of the two-phase flow in the channel by fabricating an optically transparent flow field made of cyclic olefin copolymer (COC). We introduce an in situ method to quantify clamping-induced flow channel intrusion of the diffusion layer by employing a Tesa-Visio 300 video measuring instrument. A maximum intrusion of 50 μm in the middle of the channel is measured.

We compare blocking bubble behaviour in a native, hydrophobic COC channel to a channel coated with hydrophilic PDMAA-BP at average methanol solution velocities of up to 16.3 mm s^{-1}. We use the same hydrophilic diffusion layer in both cases. The bubble in the hydrophilic channel shows almost no pinning and thus travels at approximately the same mean velocity as the fuel. In contrast to this, a blocking bubble in the hydrophobic channel pins to the channel wall at low mean fuel velocities and requires considerable fuel velocities to reach its tear-off point, which depends on the bubble length. The critical fuel velocities were in the range of 0.5 mm s^{-1} for the longest and 2 mm s^{-1} for the shortest bubble studied in this work. The receding contact angle at the front and the advancing contact angle at the back of a blocking bubble induce a significant pressure gradient along the bubble. This gradient leads to a relative velocity between mean fuel velocity and blocking bubble which is approximately constant, even at fuel velocities inside a flow channel that do not allow any bubble pinning.

To improve the understanding of bubble dynamics, a CFD/analytical model is developed that describes fuel transport around CO_2 bubbles. The model is validated and excellent agreement with the experimentally measured bubble velocity is achieved. We use the model to quantify the average fuel velocity of methanol solution bypassing a blocking bubble. This amounts

to 74 mm s^{-1} for the smallest bubble in the hydrophobic channel investigated in this work, which is considerably higher than the average fuel velocity in the flow channel. This leads to the following conclusions when designing flow fields and diffusion layers for actively pumped DMFCs.

The losses in these systems must be evaluated carefully. On the one hand, a significant fraction of the generated energy is wasted on operating a fuel supply pump which is strong enough to overcome the pressure losses of the two-phase flow in the fuel supply channels. In some cases it is advisable to employ a hydrophilic flow field to minimise the total pressure drop und thus open up the possibility to downgrade to a pump with lower power consumption. On the other hand, it can be more favourable to employ the bubble bypass configuration introduced in this work. We combine a flow channel surface with a receding contact angle of $\geq 45^\circ$ and a diffusion layer with a receding contact angle close to 0°. In this configuration, fuel bypass channels are automatically generated in a favourable position underneath a blocking bubble next to the diffusion layer. At the same time, no bypass channels exist above the blocking bubble away from the diffusion layer. This forces fuel to bypass the bubble at a high relative velocity close to the diffusion layer, which is very efficient for supplying fresh fuel to the DMFC. The pressure drop, which drives fuel through these bypass channels at considerably higher speed than the average channel velocity, results from the contact angle hysteresis at the channel walls and floor and significantly enhances mass transfer in the DMFC.

In recent years, passive DMFC systems have become increasingly popular. Obviously, these systems do not have any pumping losses, but they are limited instead by a mediocre power density due to high mass transfer losses. This case considerably favours hydrophobic walls and a hydrophilic diffusion layer to direct backflow along the diffusion layer, as the bubble rises due to buoyancy, thus enhancing mass transfer.

Acknowledgements

This work is part of the project PEM-Ca-D (Grant No. 03SF0360D) and is funded by the German Ministry of Education and Research (BMBF).

References

[1] R. Rashidi, I. Dincer, G.F. Naterer, P. Berg, Journal Power Sources 187 (2009) 509–516.
[2] A. Heinzel, V.M. Baragán, Journal Power Sources 84 (1999) 70–74.
[3] P. Argyropoulos, K. Scott, W.M. Taama, Journal of Applied Electrochemistry 2 (1999) 661–669.
[4] D. Gerteisen, Journal of Applied Electrochemistry 37 (2007) 1447–1454.
[5] H. Yang, T.S. Zhao, Q. Ye, Journal of Power Sources 142 (2005) 117–124.
[6] J. Nordlund, C. Picard, E. Birgersson, M. Vynnycky, G. Lindbergh, Journal of Applied Electrochemistry 34 (2004) 763–770.
[7] G.Q. Lu, C.Y. Wang, Journal of Power Sources 134 (2004) 33–40.
[8] H. Yang, T.S. Zhao, Q. Ye, Journal of Power Sources 139 (2005) 79–90.
[9] C.R. Buie, J.G. Santiago, International Journal of Heat and Mass Transfer 52 (2009) 5158–5166.
[10] E.N. Wang, S. Devasenathipathy, H. Lin, C.H. Hidrovo, J.G. Santiago, K.E. Goodson, T.W. Kenny, Experiments in Fluids 40 (2006) 847–858.
[11] T.T. Huang, D.G. Taylor, K.S. Lim, M. Sedlak, R. Bashir, N.S. Mosier, M.R. Ladisch, Langmuir 22 (2006) 6429–6437.
[12] N. Ichikawa, K. Hosokawa, R. Maeda, Journal of Colloid and Interface Science 280 (2004) 155–164.
[13] P. Garstecki, M.J. Fuerstman, H.A. Stone, G.M. Whitesides, Lab on a Chip 6 (2006) 437–446.
[14] T. Cubaud, M. Tatineni, X. Zhong, C.M. Ho, Physical Review E72 (2005) 037302.
[15] R. Xiong, M. Bai, J.N. Chung, Journal of Micromechanics and Microengineering 17 (2007) 1002–1011.
[16] M.J. Fuerstmann, A. Lai, M.E. Thurlow, S.S. Shevkoplyas, H.A. Stone, G.M. Whitesides, Lab on a Chip 7 (2007) 1479–1489.
[17] Y. Zhu, K. Petkovic-Duran, Microfluidics and Nanofluidics 8 (2010) 275–282.
[18] Q. Ye, T.S. Zhao, Journal of Power Sources 147 (2005) 196–202.
[19] N. Paust, C. Litterst, T. Metz, M. Eck, C. Ziegler, R. Zengerle, P. Koltay, Microfluidics and Nanofluidics 7 (2009) 531–543.
[20] N. Paust, S. Krumbholz, S. Munt, C. Müller, P. Koltay, R. Zengerle, C. Ziegler, Journal of Power Sources 192 (2009) 442–450.
[21] X. Shan, H. Chen, Physical Review E 47 (3) (1993) 1815–1819.
[22] P.B. Warren, Physical Review E 68 (6) (2003) 066702.
[23] M.J.P. Nijmeijer, C. Bruin, A.F. Bakker, J.M.J. Vanleeuwen, Physical Review A 42 (10) (1990) 6052–6059.
[24] P.D.M. Spelt, Journal of Computational Physics 207 (2005) 389–404.
[25] M. Renardy, Y.Y. Renardy, J. Li, Journal of Computational Physics 171 (2001) 243–263.
[26] C. Fang, C. Hidrovo, F. Wang, J. Eaton, K. Goodson, International Journal of Multiphase Flow 34 (2008) 690–705.
[27] Z.H. Wang, C.Y. Wang, Journal of The Electrochemical Society 150 (2003) A508–A519.
[28] W.W. Yang, T.S. Zhao, Electrochimica Acta 52 (2007) 6125–6140.
[29] S.G. Kandlikar, Z. Lu, T.Y. Lin, D. Cooke, M. Daino, Journal of Power Sources 194 (2009) 328–337.
[30] I.S. Hussaini, C.Y. Wang, Journal of Power Sources 195 (2010) 3830–3840.
[31] V. Neburchilov, J. Martin, H. Wang, J. Zhang, Journal of Power Sources 169 (2007) 221–238.
[32] Y.S. Hwang, S.W. Cha, H. Choi, D.Y. Lee, S.Y. Kim, Journal of Fuel Cell Science and Technology 6 (2009) 011023.
[33] P. van Remoortere, P. Joos, Journal of Colloid and Interface Science 141 (1991) 348–359.
[34] M. Bracke, F. De Voeght, P. Joos, Progress in Colloid and Polymer Science 79 (1989) 142–149.
[35] P. Concus, R. Finn, Acta Mathematica 132 (1974) 177–198.
[36] T.D. Blake, Journal of Colloid and Interface Science 299 (2006) 1–13.
[37] H. Bruus, Theoretical Microfluidics, 1st ed., Oxford University Press, Oxford, 2008.
[38] www.esi-cfd.com, 2011.